

CORRELATION PATTERNS IN CHARACTERISTICS OF SPATIALLY VARIABLE SEISMIC GROUND MOTIONS

A. ZERVA* AND O. ZHANG†

Department of Civil and Architectural Engineering, Drexel University, Philadelphia, PA 19104, U.S.A.

SUMMARY

A methodology for the investigation of the spatial variation of seismic ground motions is presented; data recorded at the SMART-1 dense instrument array in Lotung, Taiwan, during Events 5 and 39 are used in the analysis. The seismic motions are modeled as superpositions of sinusoidal functions, described by their amplitude, frequency, wavenumber and phase. For each event and direction (horizontal or vertical) analysed, the approach identifies a coherent, common component in the seismic motions at all recording stations, and variabilities in amplitudes and phases around the common component sinusoidal characteristics, that are particular for each recording station. It is shown that the variations in *both* the amplitudes and the phases of the motions at the station locations around the common component characteristics contribute significantly to the spatially variable nature of the motions, and, furthermore, they are correlated: increase in the variability of the amplitudes of the motions recorded at individual stations around the common amplitude implies increase in the variability of the phases around the common phase. The dispersion range of the amplitude and phase variability around their corresponding common components appear also to be associated with physical parameters. The spatially variable arrival time delays of the waveforms at the stations due to their upward travelling through the site topography, in addition to the wave passage delays identified from signal processing techniques, constitute another important cause for the spatial variation of the motions; their consideration in the approach facilitates also the identification of the correlation patterns in the amplitudes and phases.

KEY WORDS: seismic ground motions; dense instrument arrays; spatial variability; coherent component; amplitude and phase variability correlation patterns

1. INTRODUCTION

The spatial variability of seismic ground motions has an important effect on the response of lifelines, such as bridges, pipelines and communication transmission systems. It results from the apparent propagation of the waveforms on the ground surface and the differences in their shape at the various locations. The description of the spatial variability is based on probabilistic-regression-analyses of recorded data at dense instrument arrays. Commonly, the more well understood phenomenon of the apparent propagation of the motions on the ground surface is considered independently of the other causes of spatial variability. The main descriptor of the remaining causes of spatial variability is the coherence, defined as the ratio of the square of the cross-spectrum of the motions at two recording stations divided by the product of the power spectra at the two stations. Coherence estimates are insensitive to amplitude differences;¹ consequently, the variability in the motions described by the coherence is attributed mainly to their phase differences at the various locations. The power spectra of the motions, which are proportional to the square of the amplitude, are, generally, assumed to be the same at all locations. The analyses of recorded data has indicated that coherence is a function exponentially decaying with separation distance and frequency. However, different expressions and degrees of exponential decay fit data recorded at different sites or at the same site but for different earthquakes; as a result, there is a multitude of spatial variability expressions in the literature (e.g. References 2–12). It is being examined recently whether generic models can reproduce the spatially variable nature of

* Associate Professor

† Graduate Research Assistant

seismic motions at different sites and various events. Some studies^{3,10} suggest that such models may be feasible, whereas others¹¹ suggest that they may not.

Simulations of spatially variable seismic ground motions are also, generally, performed according to this same amplitude variable phase concept. Some of these analyses consider that the entire time histories are realizations of random fields (e.g. References 5 and 13), some separate them into a deterministic, propagating component and noise (e.g. Reference 14), while others simulate their spatially variable nature mainly by allowing the differences of the Fourier phases between locations to vary randomly (e.g. Reference 15). Investigations on amplitude variability started only recently: Abrahamson *et al.*³ and Schneider *et al.*¹¹ evaluated the difference between the logarithms of the spectral amplitudes between two stations and observed that it increased with increasing frequency and approached constant values at higher frequencies.

The present approach investigates the spatial variation of seismic ground motions from a different perspective. Because conventional approaches evaluate the spatial variability based on regression analyses of data with large scatter, any correlation of coherence with physical parameters may be difficult to recognize; also, the assumption that mainly the phase variation of the seismic motions contributes to their spatially variable nature or that the variations in amplitudes and phases of the motions are independent, when they may—in part—be attributed to the same physical causes, may not be totally realistic. Therefore, the approach adopted avoids statistical-regression-estimates and analyses the amplitude and phase variation of the seismic motions simultaneously.

The methodology is applied to seismic ground motions recorded during the earthquakes of 21 January 1981, (Event 5, $M_L = 6.3$), and of 16 January 1986, (Event 39, $M_L = 6.5$), at the SMART-1 array in Lotung, Taiwan. At the time of the earthquakes, the array consisted of a centre seismograph (C00), and 36 additional ones arranged on three concentric circles, the inner denoted by *I*, the middle by *M*, and the outer by *O*, with radii of 0.2, 1 and 2 km, respectively (Figure 1). The analyses of the strong motion shear (S-) wave windows in the N–S direction of both events are presented herein; for illustration purposes the vertical, compressional (P-) wave window of Event 5 is also presented. The window length in all cases is 5.12 s with a time step of $\Delta t = 0.01$ s; the starting time, however, differs so that the strong motion part of the respective wave in each

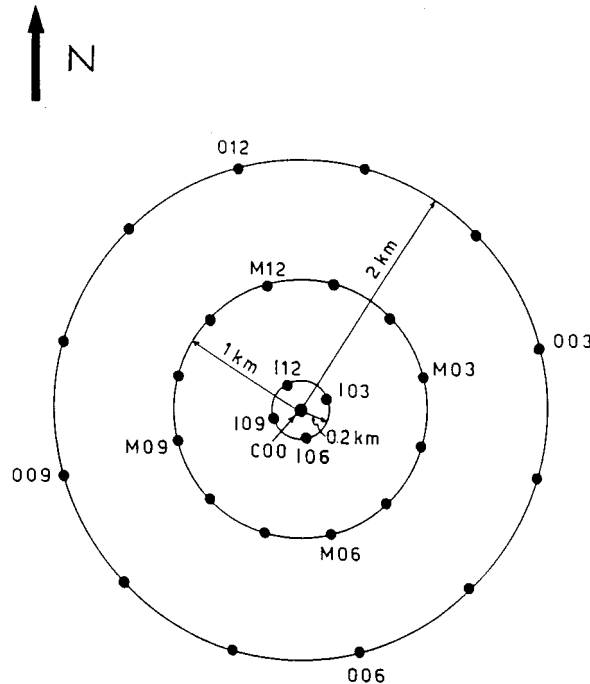


Figure 1. The SMART-1 array

direction is captured. The analyses of the E–W strong S-wave motions of both events and the vertical P-wave motions of Event 39 are described in Reference 16.

In the present approach, signal processing techniques are initially applied to the recorded data in order to identify their apparent propagation characteristics for each event and direction analysed. The seismic motions are modelled as superpositions of sinusoidal functions, described by their amplitude, frequency, wave number and phase. A computationally efficient least-squares minimization scheme is then utilized to minimize the residue between analytical motions and recorded data; the analysis estimates the amplitude and phase of the signals. Common signal characteristics (amplitude and phase) in the seismic motions are identified from the application of the approach to a number of array stations. The common signal represents a coherent wave train that propagates with the identified velocity on the ground surface and approximates to a very satisfactory degree the actual motions. The differences between the recorded data and the coherent estimates constitute the spatial variation of the motions, and are caused by arrival time delay perturbations at the array stations associated with the upward travelling of the waves through the site topography, in addition to the broad-band wave propagation delays, and by variabilities in both the amplitudes and the phases of the sinusoidal signals, identified from the application of the least-squares minimization scheme to the data recorded at one station at a time, around the common component characteristics. It is shown that the variabilities in amplitudes and phases identified at individual stations around the common component amplitude and phase are correlated and, qualitatively, associated with physical parameters.

2. SLOWNESS SPECTRA OF THE MOTIONS

Signal processing techniques for the identification of the propagation characteristics (azimuth and apparent propagation velocity) of the broad-band waves in the analysed windows are first applied to the data. From an extensive evaluation of commonly used signal processing techniques, it was determined^{16,17} that the most reliable and robust technique for the wave number estimation of a propagating broad-band signal is the conventional method,^{18–20} when used with slowness stacking.²¹ Since body waves are essentially non-dispersive, they have the same slowness \mathbf{s} at all frequencies, which specifies the direction (azimuth) of the signals through the ratio s_y/s_x , and the magnitude of their apparent propagation velocity (v_{app}) on the ground surface, since $|\mathbf{s}| = 1/v_{app}$. The (horizontal) wave number, $\boldsymbol{\kappa} = \{\kappa_x, \kappa_y\}$, of the motions is related to the slowness through $\boldsymbol{\kappa} = \omega\mathbf{s}$, with ω indicating frequency.

Stacked slowness spectra of the analysed motions of Events 5 and 39 are shown in Figure 2. The figures are contour plots: the darker the area, the higher the power of the signal (i.e. the elevation of the spectra). The darkest area (peak) identifies the slowness of the broad-band wave that dominates the motions. The spectra of the vertical P-wave window (2.0–7.12 s) and the N–S S-wave window (7.0–12.12 s) of Event 5 identified the slowness of the corresponding broad-band waves as $\mathbf{s} = (0.05 \text{ s/km}, -0.1 \text{ s/km})$ and $\mathbf{s} = (0.1 \text{ s/km}, -0.2 \text{ s/km})$, respectively (Figures 2(a) and 2(b)), i.e. the waves impinge the array at an azimuth of 153° with an apparent propagation velocity of 8.9 and 4.5 km/s for the P- and S-wave motions. These results are consistent with the source-site geometry and the apparent propagation velocity of compressional and shear waves at the site; similar results were presented by Darragh,²⁰ although for windows of half the duration of the ones analysed herein. Slowness estimates identified through stacking, as in Figure 2, represent the average characteristics of the propagation of the waves during the windows analysed. In reality, the slowness value corresponding to the highest peak in the spectra varies with frequency: In the presence of a powerful body wave the location (slowness) of the highest peak at each frequency will vary only slightly from its average location identified through stacking. The presence of waves other than the broad-band one will produce additional or dominant peaks at different slownesses at the frequencies where they contain power; the contribution of these components appears diminished in the stacked spectra. For the vertical motions analysed herein, the highest peak in the slowness spectra at essentially every frequency (within the dominant frequency range) corresponds to the slowness of the broad-band P-wave identified in Figure 2(a). For the horizontal motions, a peak appeared at essentially every frequency in the vicinity of the broad-band S-wave slowness (Figure 2(b)), but was not always the highest; therefore, the high elevation area in this direction is not so sharp as that in the vertical direction. The difference in the appearance of the spectra in the two

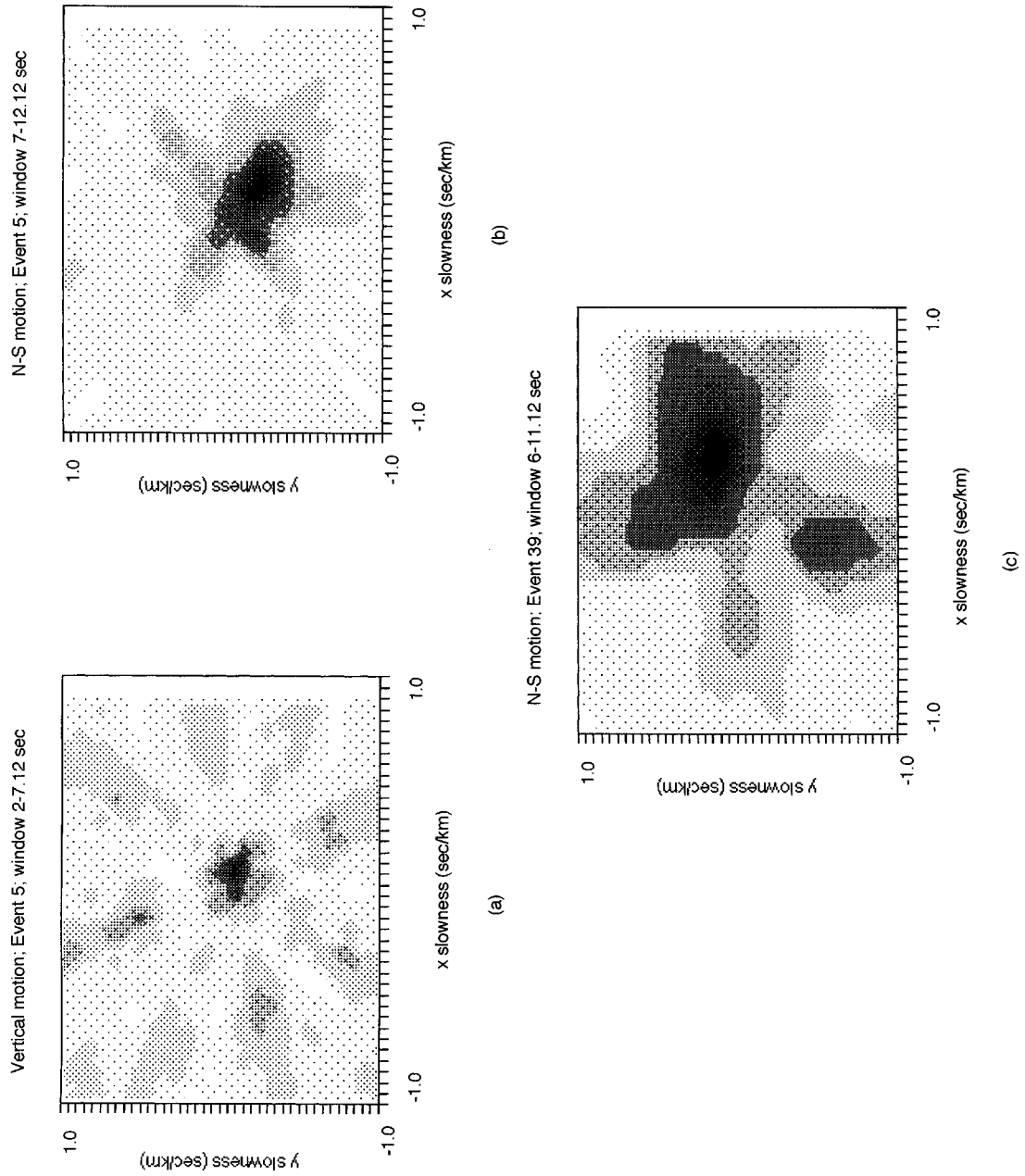


Figure 2. Slowness spectra of the motions

directions is due to the fact that the P-waves arrive first at the ground surface, and the vertical motions of Event 5 in the beginning of the records (2.0–7.12 s) are controlled by the contribution of these waves. The strong S-wave horizontal motions occur later in the records (7.0–12.12 s), and contain other waves as well as scattered energy.

Stacked slowness spectra for the strong motion S-wave window (6.0–11.12 s) in the N–S horizontal direction of Event 39 are shown in Figure 2(c). The hypocenter of this earthquake was at a depth of 10 km and a distance of 22 km from the array, i.e. 15 km closer to the ground surface and 8 km closer to the array than the hypocenter of Event 5; Event 39 was also stronger than Event 5 ($M_L = 6.5$ vs. $M_L = 6.3$).²⁰ The value of the slowness corresponding to the highest peak in Figure 2(c) is $s = (0.25 \text{ s/km}, 0.15 \text{ s/km})$, indicating an azimuth of 59° with an apparent propagation velocity of 3.2 km/s, which appears to be consistent with S-waves coming from the epicentral direction. The spectra in Figure 2(c), however, are not as ‘clean’ as those of Event 5 (Figures 2(a) and 2(b)). This strong motion window contains mixtures of various wave types: Darragh,²⁰ in analysing three windows for the one analysed herein, i.e. 6.0–8.56, 7.0–9.56 and 8.0–10.56 s, suggested that in the first window (6.0–8.56 s) the peak broad-band plane wave power arrives from non-epicentral azimuths (scattered waves of high power); from 7.0–10.56 s shear as well as surface waves and scattered energy arrive at the array. The identified slowness in the N–S direction of Event 39 is then only indicative of the presence of a propagating broad-band signal.

It can be suggested that Event 5 is representative of seismic motions for which a broad-band wave clearly dominates the records in each window, whereas Event 39 is representative of motions for which mixtures of various wave types arrive simultaneously at the array.

3. IDENTIFICATION OF AMPLITUDE AND PHASE OF SIGNALS

For the complete identification of the signals it is necessary that, in addition to their propagation characteristics identified through slowness spectra analyses, their amplitude and phase be known. Let the seismic ground motions be described by p sinusoids and expressed as:

$$\hat{\psi}(\mathbf{r}, t) = \sum_{m=1}^p A_m \sin(\boldsymbol{\kappa}_m \cdot \mathbf{r} + \omega_m t + \phi_m) \quad (1)$$

in which \mathbf{r} indicates location and t is time. Each sinusoidal component is identified by its frequency and wavenumber ($\omega_m, \boldsymbol{\kappa}_m$); A_m and ϕ_m are the amplitude and phase shift, respectively, of the signal. It is noted that no noise component is superimposed to the ground motion estimate of equation (1).

The amplitudes, A_m , and phases, ϕ_m , of the signals are determined from the system of equations resulting from the least-squares minimization of the error function between the recorded time histories $\psi(\mathbf{r}, t)$ and the approximate ones $\hat{\psi}(\mathbf{r}, t)$ (equation (1)) with respect to the unknowns A_m and ϕ_m .^{17, 22}

$$E = \sum_{i=1}^L \sum_{j=1}^N (\psi(\mathbf{r}_i, t_j) - (\hat{\psi}(\mathbf{r}_i, t_j)))^2 \quad (2)$$

evaluated at discrete locations (stations) i and times j ; $N \Delta t$ is the duration of the window analysed and Δt is the time step. Any number L of stations—ranging from one to the total number of recording stations—can be used for the evaluation of the signal amplitudes and phases. A computationally efficient approach for the evaluation of the amplitudes and phases of the signals (A_m, ϕ_m), $m = 1, \dots, p$, has been developed in the course of this study.^{17, 22} When $L > 1$ in equation (2), the approach identifies one set of amplitudes and phases per frequency (A_m, ϕ_m), that are common for all stations considered and represent the common signal characteristics; when $L = 1$, the amplitudes and phases correspond only to the particular station analysed.

4. RECONSTRUCTION OF SEISMIC MOTIONS

Five stations ($L = 5$) are used in equation (2) for the identification of their common amplitudes and phases (equation (1)); the stations are C00, I03, I06, I09 and I12—centre station and inner ring (radius of 0.2 km)

stations of the array (Figure 1). Once the common characteristics are identified, they are substituted in equation (1) and an estimate of the motions at the stations considered is obtained. The comparison of the recorded motions with the motions resulting from the superposition of the identified signals at the stations (equation (1)) are presented in Figure 3. *(It may be noted that in this figure and all subsequent ones the amplitudes are given as dimensionless numbers; for the acceleration time histories analysed herein $2g$ corresponds to 2048 of the dimensionless amplitudes in the figures).* The superposition of the signals yields the ‘reconstructed’ motions at the array stations. One hundred sinusoidal components ($p = 100$), covering the frequency range of the motions from 0.2 to 20 Hz, are used in equation (1); no noise (random) component is added to the reconstructed signals. Since amplitudes and phases at each frequency are identical for the stations considered, the reconstructed motions represent a coherent waveform that propagates with constant velocity on the ground surface.

The actual and reconstructed motions for both events are in very satisfactory agreement (Figure 3), even though the reconstructed ones consist of only the broad-band body wave signal (equation (1)). The agreement is, however, different for the different events and directions: The vertical P-wave motions of Event 5 (Figure 3(a)) are essentially perfectly matched by the approximate ones; this is due to the fact that broad-band P-waves control the vertical motion window, as can be seen from the slowness spectra (Figure 2(a)). The comparison of the horizontal N–S S-wave motions of Event 5 (Figure 3(b)) suggests that the superimposed sinusoidal components of the common signal (equation (1)) follow closely the pattern of the actual time histories, although some differences between the recorded and reconstructed waveforms can be observed in their arrival times and amplitudes, particularly those of their higher frequency components; the latter may be attributed to the presence of wave components in addition to the broad-band S-wave, as discussed in the slowness spectra evaluation (Figure 2(b)). The Event 39 reconstructed motions (Figure 3(c)) capture the mixture of low and higher frequency dominant wave components in the recorded data. In particular, the reconstructed motions reproduce closely the recorded ones after 7.0 s, when shear and surface waves arrive at the array with close azimuths and apparent propagation velocities,²⁰ but not so well between 6 and 7.0 s, when scattered energy arrives at the array from non-epicentral directions.²⁰ This behaviour of the reconstructed motions may be attributed to the fact that the value of the slowness used in the least-squares minimization scheme was obtained from spectra that were controlled by the more powerful shear and surface waves (Figure 2(c)), so that the propagation pattern of the scattered waves in the first few seconds of the window was not well reproduced.

Figure 3 indicates that the reconstructed motions reproduced to a very satisfactory degree the actual ones, even though they consist of only the broad-band coherent body wave signal (equation (1)). This suggests that a common signal truly exists in the records and this coherent motion can describe the major characteristics (overall apparent propagation and amplitude, and zero crossing rate) of the data. However, the details in the actual motions are not matched by the reconstructed ones; these details constitute the spatially variable nature of the motions, and include variabilities in the arrival time, the amplitude and the higher frequency content of the wave components in the approximate motions compared to the actual ones.

5. VARIATION OF AMPLITUDES AND PHASES

When only one station at a time ($L = 1$ in equation (2)) is used in the evaluation of amplitudes and phases at different frequencies for that particular station, the reconstructed motion is indistinguishable from the recorded one. This does not necessarily mean that the analysed time histories are composed only of the identified broad-band waves, but rather that the sinusoidal functions of equation (1) can match the sinusoidally varying seismic time histories, i.e. equation (1) becomes essentially compatible to a Fourier transform. However, significant deviations in the values of the amplitudes and phases evaluated at each station from the common ones suggest the effect (amplification and phase modification) of the upward propagation of the waves through the site topography, the contribution of wave components other than or in addition to the broad-band wave and/or the presence of scattered energy. Thus, the comparison of the results at the individual stations with the common ones provides insight into the causes for the spatial variation of seismic ground motions. It is noted that the effect of the apparent propagation of the motions with constant

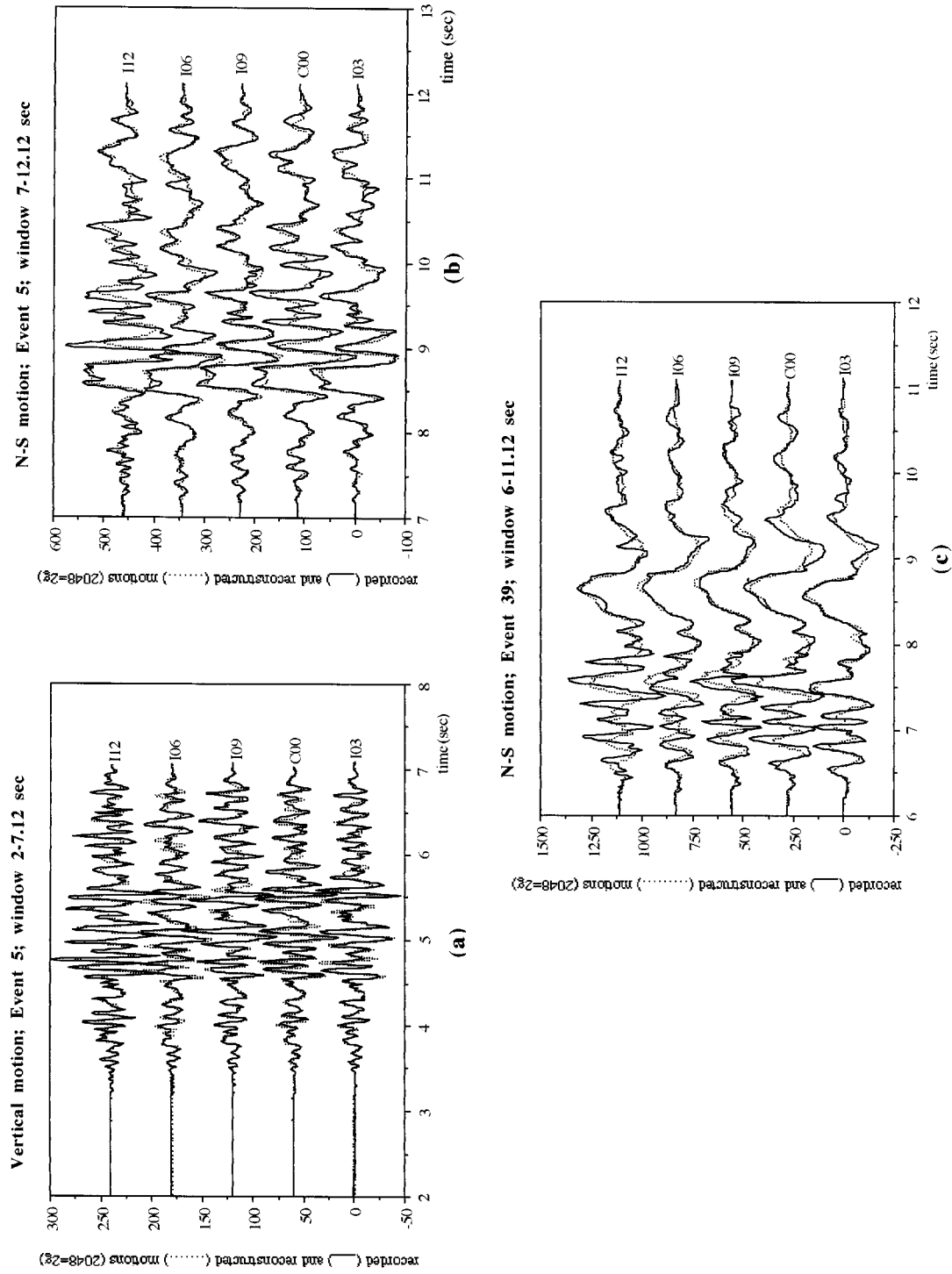


Figure 3. Comparison of recorded and reconstructed motions at the centre and inner ring stations of the array

velocity on the ground surface has been taken into consideration through the term $\kappa_m \cdot \mathbf{r}$ in the seismic ground motion approximation (equation (1)).

Figure 4 presents the amplitude and phase variation of the sinusoidal components of the motions in the horizontal (N–S) direction for Events 5 and 39; the continuous, wider line in these figures, as well as in the subsequent ones, indicates the common signal characteristics, namely, the contribution of the identified body wave to the motions at all five stations, whereas the thinner, dashed lines represent the corresponding amplitudes and phases when one station at a time is considered in equation (2). The differences in the characteristics of the seismic ground motions caused by the two earthquakes can be clearly seen in the figure: Higher amplitudes and dominance of lower frequency components are obtained from the more powerful Event 39 motions (Figure 4(c)) compared to those of Event 5 (Figure 4(a)). In the lower frequency range (< 1.5 Hz) and for both events, amplitudes and phases identified at the individual stations essentially coincide with the common component. As frequency increases in the range of 1.5–4 Hz for Event 5 and 1.5–3 Hz for Event 39, the common amplitude represents the average of the site amplification and phases start deviating from the common phase. It should be noted that the values of the phases were restricted in the range of $[0, 2\pi)$, and, therefore, jumps of approximately 2π are not indicative of a drastic variation in the phases. At higher frequencies, the common amplitude becomes lower than the ones identified at the stations and phases vary randomly; this behaviour is shown in Figure 4 only up to 15 Hz—and not up to the cutoff frequency of 20 Hz used in the analysis—so that the amplitude and phase variabilities over the significant (lower) frequency range of the motions can be observed more clearly.

Part of the variabilities around the common components in Figure 4—in addition to possible scattering effects and the contribution of waves other than the broad-band one—may be due to the fact that an absolutely constant slowness was used for the propagation of the sinusoidal components at all frequencies, due to inaccuracies in the estimation of the slowness s of the motions, and, also, because the time history approximation (equation (1)) does not allow for time delay perturbations in the arrival of the waves at the various stations due to their upward travelling through horizontal variations of the geologic structure underneath the array; these effects influence phases more directly than amplitudes, as can be deduced from equation (1), and are also apparent in the comparison of the actual and reconstructed motions.

The effect of the use of constant slowness in the sinusoidal estimates (equation (1)) is that part of the reconstructed motions arrives earlier or later than the corresponding part of the actual ones, as, e.g. the earlier and later arrival of the waveforms during the initial 2 s of the N–S window of Event 39 at stations *I06* and *I12*, respectively (Figure 3(c)). This is due to the fact that the S- and surface wave slowness is used in the least-squares minimization scheme of the Event 39 motion approximation, that does not correspond to the higher frequency, scattered energy propagation pattern in the first 2 s of the window (Figures 2(c) and 3(c)). As a result, the phases identified at the individual stations for this event (Figure 4(d)) start varying significantly around the common phase at a frequency (≈ 2 Hz) that is significantly lower than the frequency at which a similar behaviour is observed for the Event 5 phases (≈ 4 Hz in Figure 4(b)), for which the propagation characteristics were more consistent with those of a broad-band signal throughout the entire window. The use of the actual slowness of the waves identified at each frequency would reduce this effect,¹⁶ but, due to its detailed and event specific nature, would not be helpful in establishing general descriptions for the spatial variability.

The effect of an inaccurate slowness estimate and/or an additional time delay due to the upward travelling of the waves through the site topography, that may be particular for each station, appears as an earlier or later arrival of the entire reconstructed time history compared to the actual one (e.g. the earlier arrival of the reconstructed vertical P-wave motions of Event 5 at station *C00*, or the later arrival of the N–S S-wave motions of the same event at station *I12* in Figures 3(a) and 3(b), respectively). The contribution of these effects to the phases is proportional to the frequency, since both the slowness ($\kappa = \omega s$) and the additional time delay are multiplied by the frequency in the sinusoidal estimate of the motions (equation (1)); hence, it is small at low frequencies and increases with increasing frequency (Figure 4). If phases in Figure 4 were allowed to assume values outside the $[0, 2\pi)$ range by adding to their values the smallest integer multiple of 2π that would produce a monotonically increasing function of phase with frequency, then an inaccurate slowness estimate and/or an additional time delay would cause the phases at the individual stations to

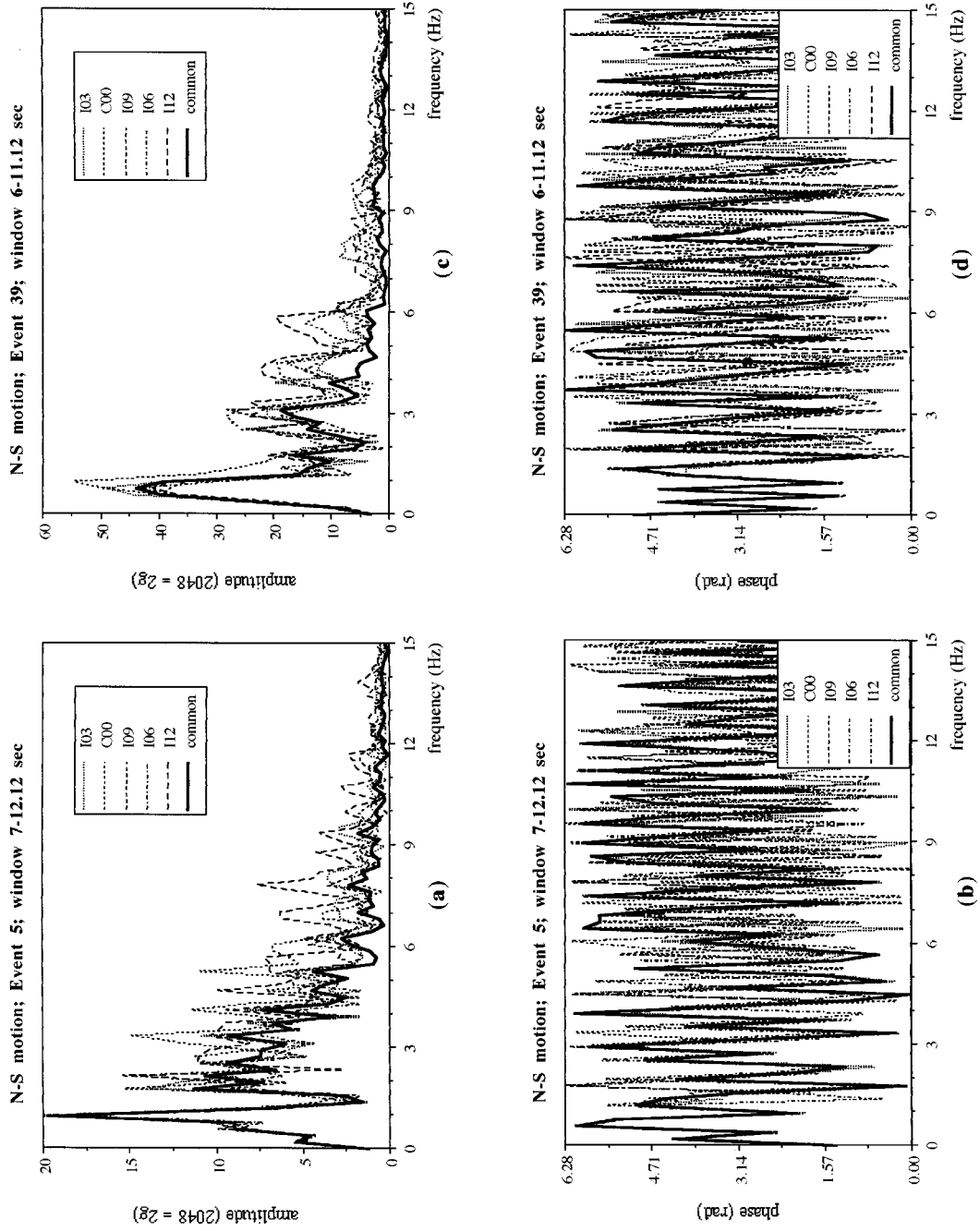


Figure 4. Amplitude and phase variation of the strong S-wave motions in the N-S direction of Events 5 and 39 at the centre and inner ring stations

envelope from above and below the common phases with increasing distance as frequency increases; this behaviour may not be easily recognized in the figure due to the $[0, 2\pi)$ restriction. Although inaccuracies in the slowness estimate may be difficult to avoid, due to limited recorded information in space and the dependence of the results on the array configuration, the contribution of the time delay due to the upward propagation of the waves can be reduced by aligning the seismic motions.

6. ALIGNMENT OF TIME HISTORIES

An approach to estimate the arrival of a broad-band wave at the individual stations relative to a reference station is through alignment, i.e. time shift of the time histories so that the propagation effect is removed. In this process, the cross-correlation of the motions relative to a reference station is evaluated; the time corresponding to the highest correlation provides the delay in the arrival of the waves at the various stations relative to their arrival at the reference one. Tables I(a) and I(b) present the alignment delays in time increments for stations *I03*, *I06*, *I09* and *I12* of the inner ring, and for stations *M03*, *M06*, *M09* and *M12* of the middle ring of the array with respect to *C00* (Figure 1); positive values for the alignment indicate that the ‘motion’ arrives earlier at the stations than at *C00*, and negative values that it arrives later.

The time delays in the table do not generally agree with the propagation pattern of the broad-band waves coming from the epicentral directions of the earthquakes, identified in the slowness spectra analyses. The azimuth of Event 5 is in the second quadrant and that of Event 39 in the first (Figures 1 and 2). For Event 5, the motions would then arrive first at the ‘second quadrant’ stations (*M03*, *M06*, *I03* and *I06* in Figure 1) and later at the ‘fourth quadrant’ ones (*I09*, *I12*, *M09* and *M12*), whereas, for Event 39, they would arrive first at the ‘first quadrant’ stations (*M03*, *M12*, *I03* and *I12*) and later at the ‘third quadrant’ ones (*I06*, *I09*, *M06* and *M09*). However, the time delays relative to *C00* obtained from the alignment analyses (Table I) do not follow these patterns and exhibit a random behaviour. The reason for these differences is that the broad-band wave characteristics obtained from the slowness stacking analyses represent the average propagation of the motions over the entire array. On the other hand, the alignment process identifies possible delays in the arrival of the waves between two stations that are caused by their average propagation pattern, by their upward travelling through the site topography and by random effects, i.e. it presents a detailed, local picture of the wave propagation differences between stations. It should be emphasized, however, that when the time delays for maximum correlations are evaluated for the motions at all stations, an average propagation pattern of waves across the array can be recognized, that is compatible with the one identified from the slowness analyses;²² this is due to the fact that—on the average—the physical concepts underlying both approaches are the same: both consider that the entire waveform propagates at a certain azimuth with constant velocity.

The comparison in Figure 3 of the arrival times at the array stations of the reconstructed motions, which propagate with constant velocity on the ground surface, with those of the recorded data, which incorporate the delays due to the upward travelling of the waves through the site topography (Table I(a)), suggests that these additional delays contribute significantly to the spatially variable nature of the motions; the same observation was also made in References 1, 6 and 23. In addition to this direct effect of the time delays on the spatial variability of the motions, their consideration in the present analysis affects the picture of the amplitude and phase variation, as discussed in the following section.

Table I. Alignment delays (in time increments of Δt ; $\Delta t = 0.01$ s) of motions at array stations relative to *C00*

Direction	Event	Window (s)	(a) Inner ring stations					(b) Middle ring stations				
			<i>I03</i>	<i>C00</i>	<i>I09</i>	<i>I06</i>	<i>I12</i>	<i>M03</i>	<i>C00</i>	<i>M09</i>	<i>M06</i>	<i>M12</i>
Vertical	5	2.0–7.12	1	0	1	3	–1	4	0	8	14	16
N–S	5	7.0–12.12	2	0	0	4	1	10	0	10	32	14
N–S	39	6.0–11.12	8	0	1	6	–2	39	0	–28	10	25

7. COMMON COMPONENTS IN ALIGNED MOTIONS

The amplitude and phase variations of the aligned motions are examined in this section. The error function (equation (2)) is used again in the minimization scheme but, in this case, the recorded data are aligned with respect to C00, and, in the sinusoidal approximation of the motions (equation (1)), the term $\kappa_m \cdot \mathbf{r}$ is set equal to zero, since the motions arrive simultaneously at all array stations. When the motions recorded at one station at a time are used in the minimization scheme, equation (2) reduces to the Fourier transform of the aligned motions. It is emphasized that the analyses of both the aligned and the non-aligned data consider broad-band wave propagation characteristics in the motions: The analysis of the actual data considers constant slowness propagation over the entire array area, and the analysis of the aligned ones that the entire waveform propagates with constant velocity between station pairs, but the propagation velocity is different for the different station pairs.

Figures 5–7 present the variations of the amplitudes and phases of the aligned motions during the vertical P-wave window of Event 5, and the horizontal N–S S-wave windows of Events 5 and 39, respectively. Again, for clarity purposes, the amplitude and phase variations are presented up to a frequency of 15 Hz rather than up to the cutoff frequency of 20 Hz used in the analysis. Parts (a) and (b) in the figures present the common characteristics (amplitude and phase, respectively) determined from the application of the least-squares minimization scheme to the aligned motions at the five inner ring stations (*I03*, *I06*, *I09*, *I12* and *C00*), together with the amplitude and phase variation identified using one station at a time. Part (c) and (d) in the figures present again the common component amplitude and phase of the aligned motions but, instead of the inner ring stations, the middle ring ones (*M03*, *M06*, *M09* and *M12*) together with the reference station *C00* are considered in the minimization scheme, i.e. again, $L = 5$ in equation (2). The recorded aligned motions at stations *M03*, *M06*, *M09* and *M12* are then analysed individually, and the variation of their amplitudes and phases together with those identified at *C00* are also presented in the figures.

The analysis of the vertical motions at the inner ring stations of Event 5 indicates that the common amplitude represents the average of the site amplification (Figure 5(a)), and that phases at the individual stations follow very closely the variability of the common phase for the entire frequency range considered (Figure 5(b)). It is recalled that the values of the phases were restricted to the range $[0, 2\pi)$, and, therefore, jumps of approximately 2π are not indicative of a drastic variation in the phases. The small variabilities of amplitudes and phases around the common component indicate the strong presence of a coherent broad-band signal. Due to the dominance of the broad-band P-wave in this window and its high propagation velocity, the amplitude and phase variability identified from the non-aligned recorded data with the constant slowness ground motion estimate (equations (1) and (2)) are very similar to those presented in Figures 5(a) and 5(b).¹⁶ Significant differences, however, are observed in the amplitude and phase variations of the N–S motions of both events identified from the analyses of the aligned and the non-aligned data (cf. Figures 6(a) and 6(b) and 7(a) and 7(b) with Figure 4), particularly for the Event 39 motions: The common amplitudes of the aligned data represent the average of the site amplification over a wider frequency range, and the amplitudes at the individual stations are more closely clustered around the common ones in the dominant frequency range of the motions. The common phases follow similar patterns whether the constant slowness approximation (Figures 4(b) and 4(d)) or the alignment procedure (Figures 6(b) and 7(b)) is used. However, over essentially the entire dominant frequency range of the motions of both events, phases identified at the individual stations are more closely clustered around the common phase when the aligned motions are used (Figures 6(b) and 7(b) compared to Figures 4(b) and 4(d)), suggesting that deviations in the actual arrival time of the waves at the individual stations from the arrival times predicted by the constant slowness wave approximation affect the variability of the phases around the common phase rather than the value of the common phase itself.

The common amplitudes and phases identified from the middle ring stations are very similar—same trend, almost identical phases, slight variabilities in the values of the amplitudes—to those of the inner ring stations (cf. parts (c) and (d) with parts (a) and (b) in Figures 5–7), particularly, considering the facts that separate analyses were performed for the two sets of stations, and that the longest separation distance for the middle ring stations is 2 km whereas that of the inner ring ones 400 m (Figure 1). Their differences are an expected

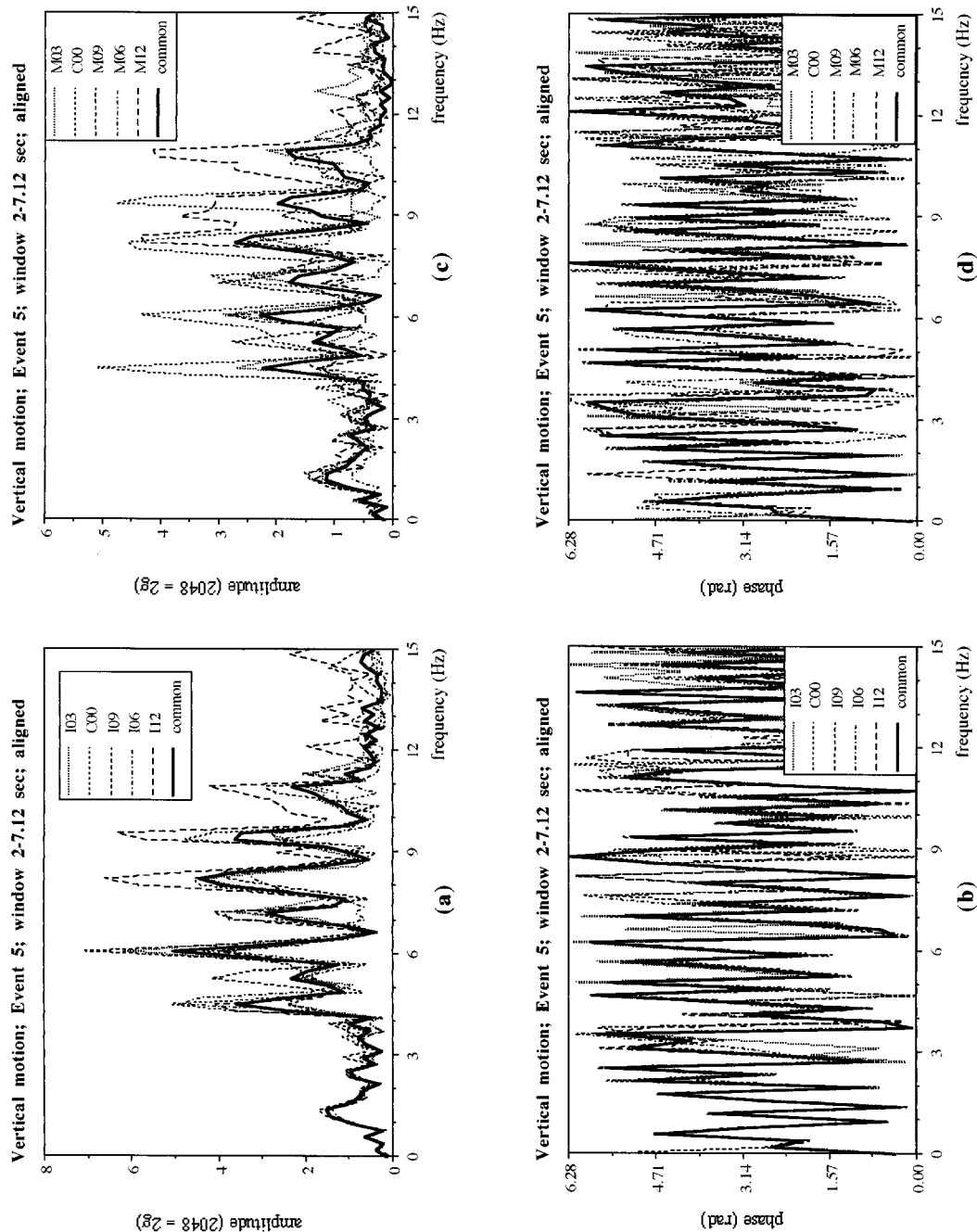


Figure 5. Amplitude and phase variation of the vertical P-wave aligned motions of Event 5 at the inner and middle ring stations, including the centre station C00

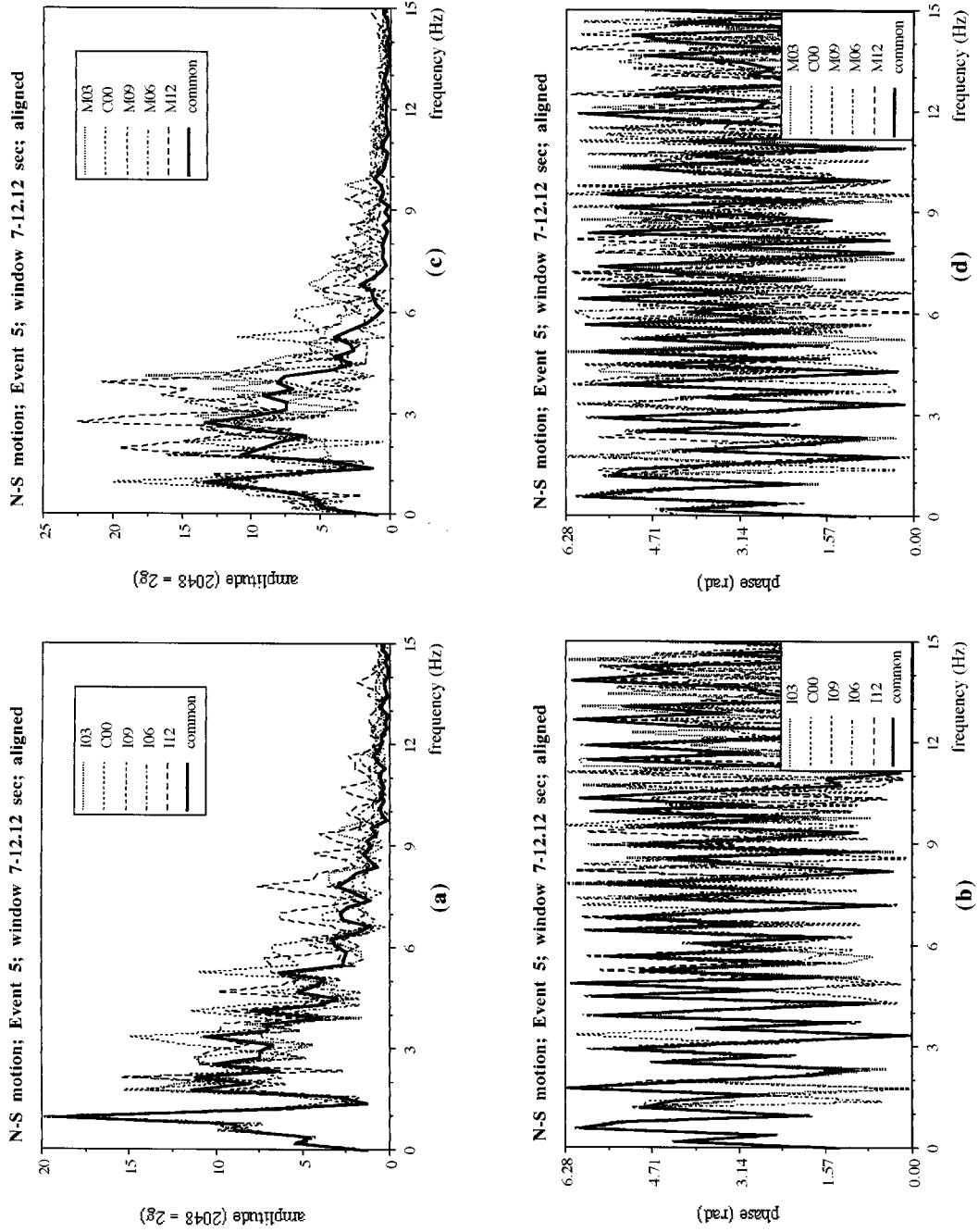


Figure 6. Amplitude and phase variation of the N-S wave aligned motions of Event 5 at the inner and middle ring stations, including the centre station C00

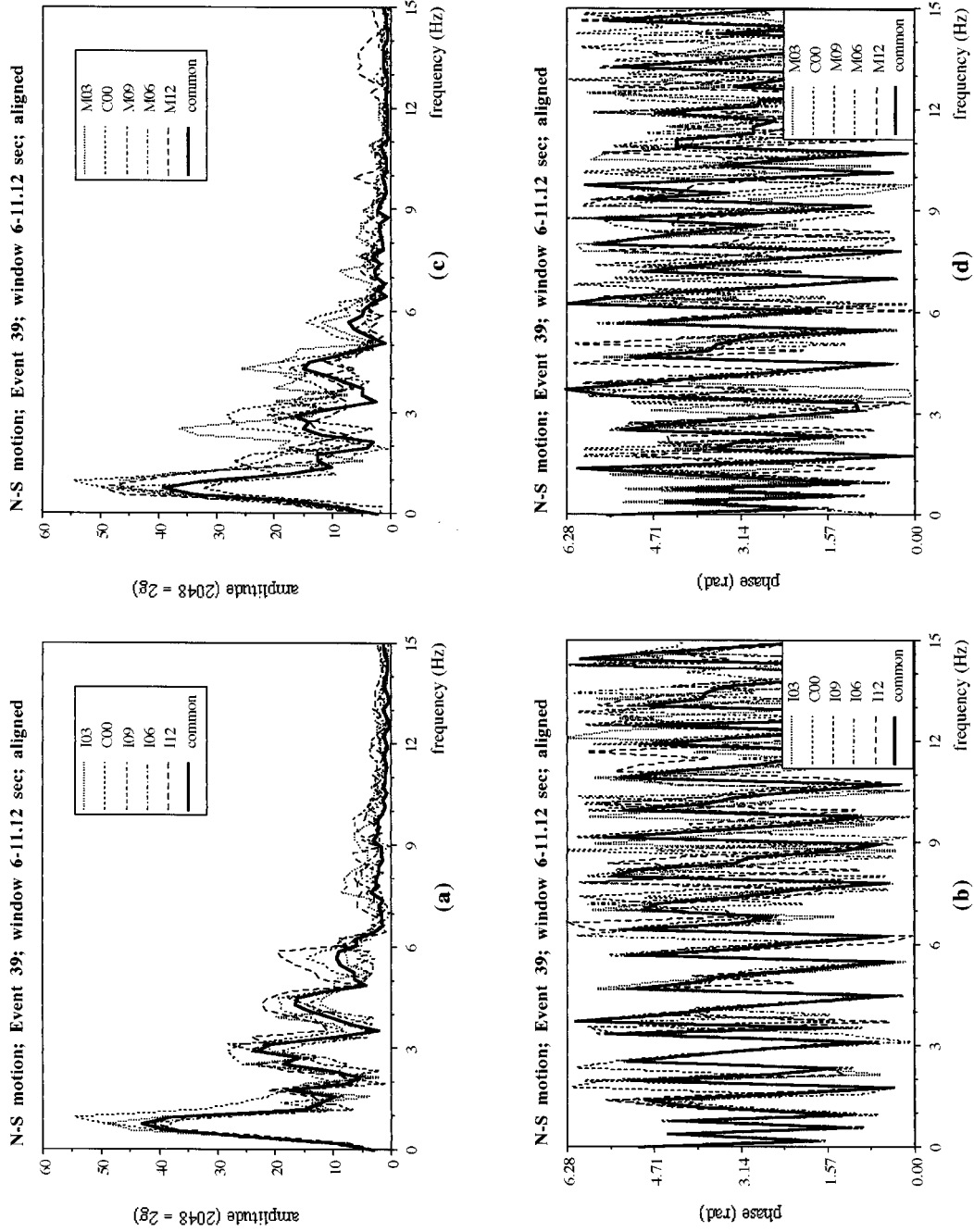


Figure 7. Amplitude and phase variation of the N-S wave aligned motions of Event 39 at the inner and middle ring stations, including the centre station C00

consequence of the larger scatter in the data at the further away stations due to attenuation of the waves and more significant variations in the site topography. The variability of the identified amplitudes and phases at the individual middle ring stations around their common components are, however, larger than those of the inner ring stations.

The agreement of the common amplitudes and phases over an extended area of radius of 1 km strongly suggests the existence of the coherent component in the data. The common amplitude can be viewed as the average amplification of the motions at the site, and is associated with the common phase variability with frequency, which resembles random distribution between $[0, 2\pi)$. The spatial variability of the motions, in addition to the propagation effects already considered, results from the derivations in both amplitudes and phases at the individual stations around the common components (Figures 5–7), which are described in the following section in terms of differential amplitudes and phases.

8. DIFFERENTIAL AMPLITUDE AND PHASE VARIABILITY

Figures 8–10 present the normalized differential amplitudes and the differential phases of the motions during the vertical P-wave window of Event 5 and the horizontal (N–S) S-wave windows of Events 5 and 39, respectively, up to the cutoff frequency of 20 Hz considered in the analysis. The normalized amplitudes (parts (a) and (c) in Figures 8–10, for the inner and middle ring station data, respectively) are obtained by subtracting at each frequency the common amplitude from the amplitudes identified at the individual stations and dividing by the common amplitude. The differential phases (parts (b) and (d) in Figures 8–10, for the inner and middle ring station data, respectively) are obtained by subtracting at each frequency the common phase from the phases identified at each station. The normalized differential amplitudes in Figures 8–10 are cut off at a maximum value of 7.5: their actual values can be significantly high, because the common component can assume low values at certain frequencies (Figures 5–7), but are not important for the analysis, as will be shown subsequently. The phase differences in Figures 8–10 are allowed to vary between $[-\pi, +\pi)$, rather than between $[0, 2\pi)$, as was the case in Figures 5–7.

It may be observed from parts (b) and (d) in Figures 8–10, that the differential phases exhibit symmetry around the zero axis, which suggests that the mean value of the actual phases over the entire frequency range is the common phase identified from all stations considered. It also appears that the range of dispersion of the differential phases, excluding the isolated peaks, is contained within envelope functions, symmetric around the zero axis. The distance of these envelope functions from the zero axis varies for the different events, directions and station separation distances (inner or middle ring). Due to the symmetry of the differential phases, only their positive envelope trend will be discussed in the following. The normalized differential amplitudes tend to increase in the positive range as frequency increases, whereas their negative values do not exceed a low value. A careful observation of parts (a) and (c) in Figures 8–10 indicates that at low frequencies, differential amplitudes, excluding again the isolated peaks, also exhibit symmetry around the zero axis; i.e. the common amplitude represents the mean of the amplitudes identified at the individual stations (parts (a) and (c) in Figures 5–7). However, as frequency increases, additional waves and/or scattered energy contribute significantly to the motions, the common amplitudes of the broad-band components become lower than the amplitudes at the individual stations, and the normalized differential amplitudes assume large positive but only low negative values. The dispersion range of the positive normalized differential amplitudes relative to the zero axis is also contained within envelope functions, that are event, direction and station separation distance dependent; the trend of these positive envelope functions will be discussed in the following. From the comparison of parts (a) and (c) with parts (b) and (d) in Figures 8–10, it follows that the trend of the envelopes of the normalized differential amplitudes is very similar to that of the differential phases:

In the lower frequency range the amplitude and phase envelope functions can be defined as straight lines parallel to and at close distances to the zero axis. For the inner ring vertical motions (Figures 8(a) and 8(b)) the frequency range, where this behaviour occurs, is wide and the distance of the envelopes from the zero axis very small. For the horizontal motions at the inner ring stations the frequency range becomes narrower and the distance of the envelope functions from the zero axis greater (Figures 9(a), 9(b), 10(a) and (b)) than those of the vertical motions. Similarly, for the middle ring station data the frequency range gets narrower and the

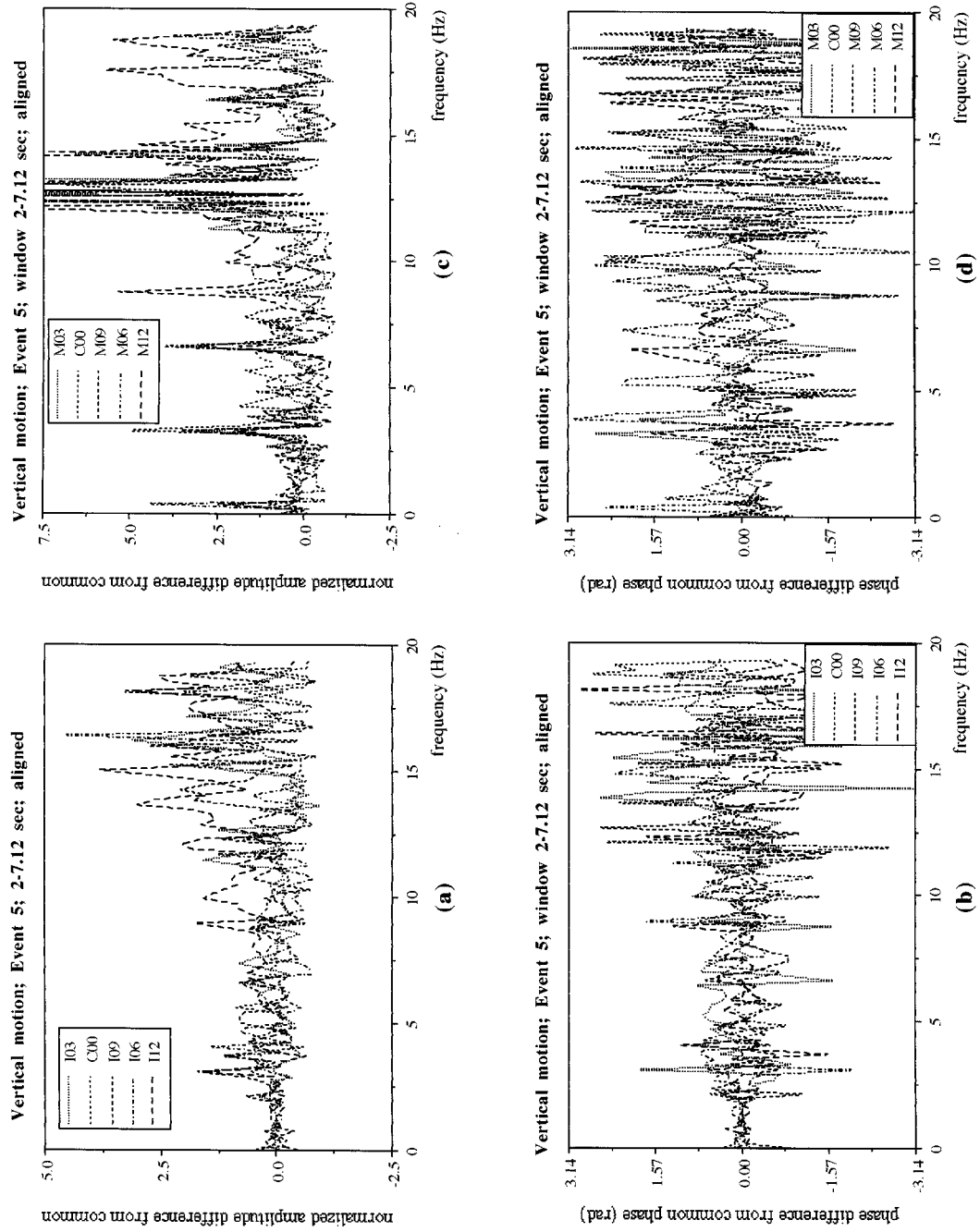


Figure 8. Differential amplitude and phase variation of the vertical P-wave aligned motions of Event 5 at the inner and middle ring stations, including the centre station C00

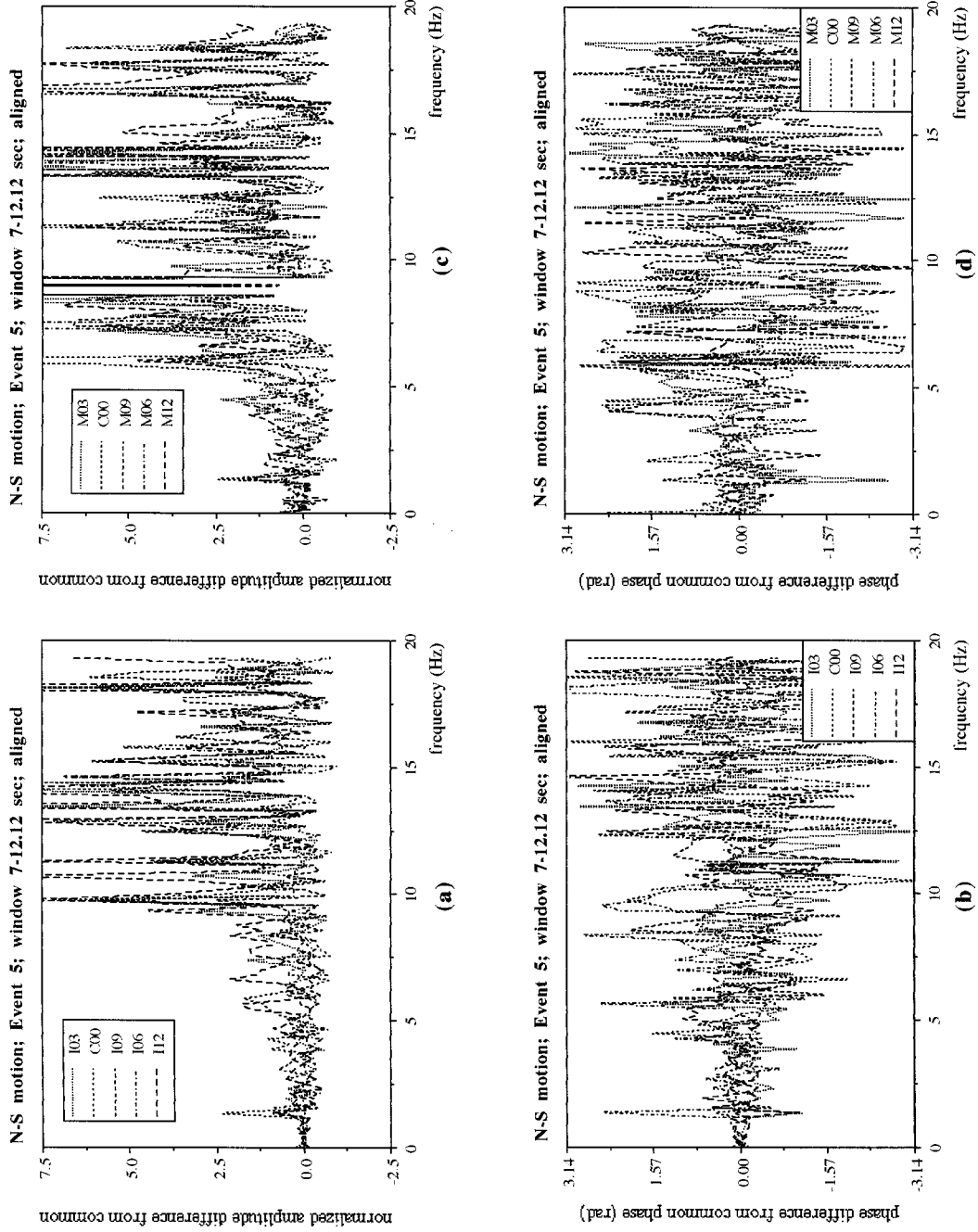


Figure 9. Differential amplitude and phase variation of the N-S S-wave aligned motions of Event 5 at the inner and middle ring stations, including the centre station C00

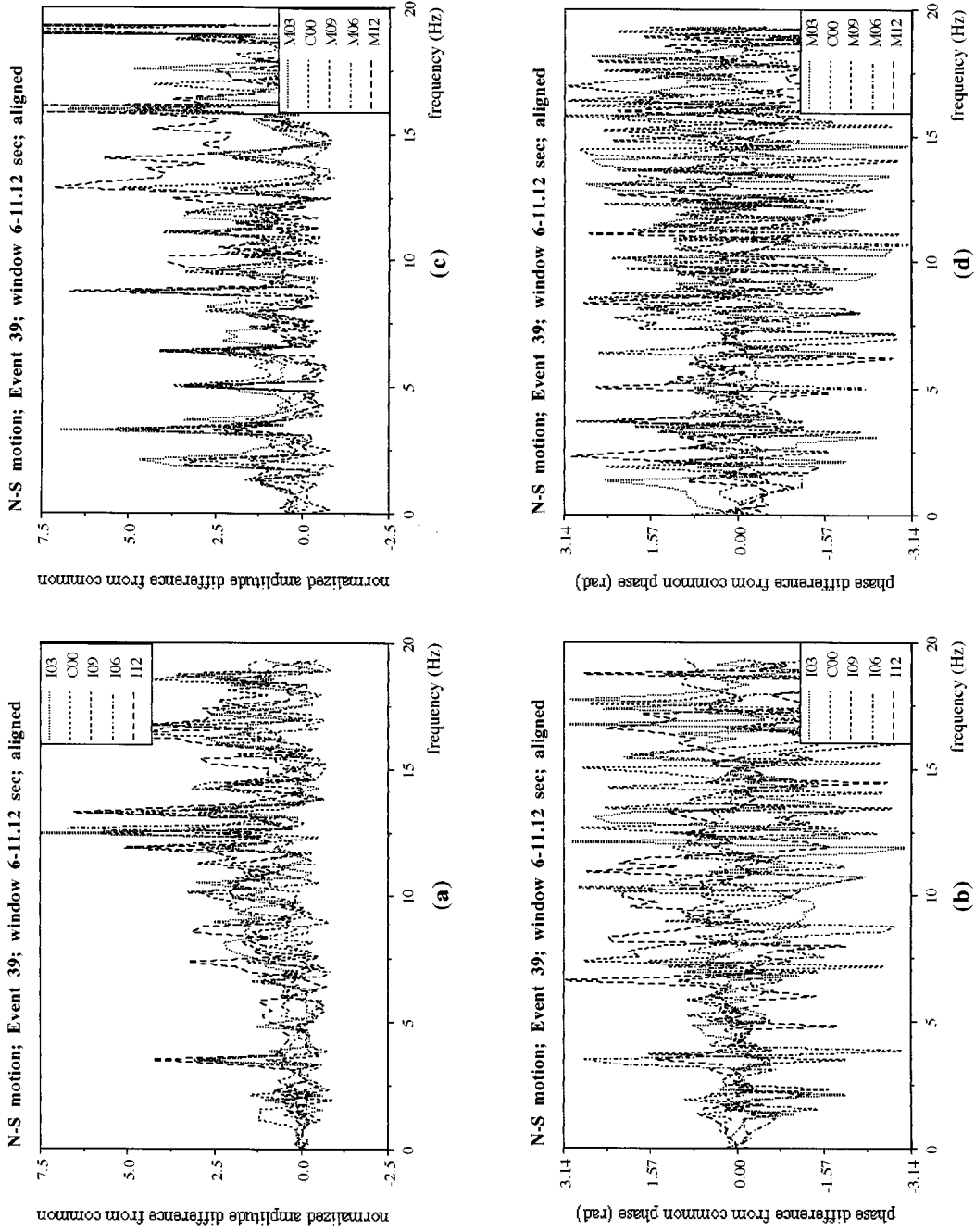


Figure 10. Differential amplitude and phase variation of the N-S S-wave aligned motions of Event 39 at the inner and middle ring stations, including the centre station C00

distance of the envelopes from the zero axis greater than those of the inner ring ones (cf. parts (c) and (d) with parts (a) and (b) in Figures 8–10). In this lower frequency range the distance of the envelopes from the zero axis can be related to the wavelength of the identified signal; it is noted that, although the motions have been aligned, the effects of the characteristics of the contributing waves cannot be removed. In the low frequency range the wavelength of the signals is long; thus, they do not see the site irregularities, particularly for the inner ring stations (radius of 200 m), and the motions appear to be coherent. The wavelength is longer for the P-waves (higher propagation velocity) than for the S-waves, and, consequently, the distance of the envelopes from the zero axis is shorter for the vertical motion windows than for the horizontal ones. The distance between stations for the middle ring area (radius of 1 km) is greater than that for the inner ring ones, and, although the wavelength at low frequencies is still long, the signals start seeing the irregularities along their propagation path. As a result, the distance of the envelope functions from the zero axis increases for these motions.

As frequency increases within the dominant site amplification frequency range of the motions, the distance of the amplitude and phase envelope functions from the zero axis increases gradually at different rates for the different directions, events and station separation distances considered; the rate is slower for the vertical motions than the horizontal ones and for the inner ring area than the middle ring one. In this range, the common signal amplitude represents the average of the amplitudes identified at the individual stations (parts (a) and (c) in Figures 5–7); it can be observed from Figures 5–10 that the closer the amplitudes at the individual stations are clustered around the common signal amplitudes, the smaller the normalized differential amplitude *and* differential phase variability around the zero axis, whereas, the wider the amplitudes at the individual stations are spread around the common signal amplitudes, the longer the distance of *both* amplitude and phase envelope functions from the zero axis. The fact that the common amplitudes reproduce the average of the amplitudes identified at the individual stations suggests that the motions are controlled by the broad-band signal; the increase in the variabilities of amplitudes and phases around the common component as frequency increases may be associated with the modifications in the amplitude and phase of the signal at the individual locations due to its upward transmission through the horizontal variations of the layers underneath the array, the decreasing wavelength of the signals at increasing frequencies and the more apparent presence of scattered energy (noise). In this dominant site amplification frequency range, there appear isolated peaks in both the normalized differential amplitude and differential phase variability at exactly the same frequencies. At these frequencies amplitudes are low and phases vary randomly (Figures 5–7), suggesting that the motions are dominated by scattered energy, as will be further elaborated in the next paragraph. This variability, however, may not be of significant consequence for the modelling or the simulation of spatially variable seismic ground motions: it occurs when amplitudes are low within the dominant frequency range of the motions.

At higher frequencies, past the dominant frequency range of the motions, the common signal amplitude no longer represents the average of the site amplification, and becomes lower than the amplitudes identified at the individual stations. This behaviour may be attributed to significant contributions of other wave components in addition to the broad-band signal, and, mainly, to the strong presence of scattered energy (noise). Because these higher frequency wave components propagate at different velocities than the broad-band signal, phases at the individual stations (parts (b) and (d) in Figures 5–7) deviate significantly from the common phase. Thus, the normalized differential amplitudes assume high values, and the phase differences vary randomly between $[-\pi, +\pi]$, i.e. the differential phase envelope functions can be considered as being parallel to the zero axis at a distance equal to π .

A peculiarity in the behaviour of the phases of Event 39 (Figure 10) ought to be pointed out: the differential phases for both the inner and the middle ring stations follow a linear trend, which is more obvious in the lower frequency range. This is due to inaccuracies in the estimation of the propagation pattern of the wave components for this event, that affect phases by increasing their value linearly with frequency, as already pointed out in Section 5; it is recalled that these windows contain a mixture of various wave types propagating with different velocities that neither the constant slowness nor the alignment approximation can fully capture. Due to the same reason, the dispersion range of amplitudes and phases for this event is larger than that of Event 5 (Figures 9 and 10).

It follows then from the above considerations that the amplitude and phase variabilities of the motions around their common, coherent characteristics are correlated and can also be, qualitatively, associated with physical parameters. The differential phase variability, as described herein, can be related with coherence estimates:¹⁶ in the low frequency range, where phases vary randomly within envelope functions that are parallel to the zero axis at close distances, coherence assumes values close to one; within the dominant frequency range of the motions, where the envelope functions increase with frequency, coherence decreases, and, finally, in the higher frequency range, where phases vary randomly between $[-\pi, +\pi)$ and noise dominates, coherence assumes zero values. It is emphasized, however, that the results of this study indicate that both amplitude and phase differential variability contribute to the spatial variation of the motions, and, furthermore, they are correlated: coherence estimates, that represent mainly phase variability, may not be a sufficient descriptor of the overall spatial variation of the motions. It should be noted at this point that the relation of coherence with differential phases, with respect, however, to the phases at a reference station rather than to the phases of the common component, has been recognized by Abrahamson.¹⁵

9. SUMMARY AND CONCLUSIONS

A methodology for the investigation of the spatial variation of seismic ground motions recorded at strong motion arrays has been presented. The data recorded at the SMART-1 array in Lotung, Taiwan, during the vertical P-wave window of Event 5, and the horizontal (N-S) S-wave windows of Events 5 and 39 have been analysed.

The approach is based on a least-squares minimization scheme, that minimizes the residue between recorded data and analytical motions; the analytical motions are sinusoidal functions, described by their amplitude, frequency, wave number and phase. The characteristics of a common, coherent component in the motions are identified by applying the method to data recorded at a number of stations for each event and direction analysed; the minimum separation distance between stations considered was 200 m and the maximum one 2 km. The common component amplitude may be viewed as the average representation of the broad-band signal characteristics at the site and is associated with the common phase which varies randomly between $[0, 2\pi)$. The coherent motions, reconstructed from the common component characteristics, are in satisfactory agreement with the actual recorded data even though they consist of only a broad-band wave that propagates with constant velocity on the ground surface. The differences between the recorded data and the coherent estimates constitute the spatial variability of the motions, and are caused by arrival time delays of the waveforms at the array stations associated with their upward travelling through the site topography, in addition to the broad-band wave propagation delays, and by variabilities in both amplitudes and phases of the sinusoidal signals, identified from the application of the least-squares minimization scheme to the data recorded at one station at a time, around the common component characteristics.

The dispersion range of the variability of the amplitudes and phases identified at the individual stations around the common amplitude and phase are correlated: In the low frequency range, the variability in both amplitudes and phases around their corresponding common values is small for the close by stations, and increases slightly for the further away ones; this behaviour may be attributed to the fact that, due to its long wavelength at low frequencies, the signal does not recognize site irregularities, particularly for the inner ring stations, and, thus the motions appear to be coherent. Within the dominant frequency range of the motions, the dispersion range of amplitudes and phases around the common components increase gradually as frequency and station separation distance increase; this behaviour may be attributed to the modifications in the amplitude and phase of the signal at the individual locations due to its upward transmission through the horizontal variations of the layers underneath the array, the decreasing wavelength of the signal at increasing frequencies and the more apparent presence of scattered energy (noise). At higher frequencies, the common amplitudes are lower than the amplitudes identified at the individual stations and phases vary randomly. This behaviour of amplitudes and phases indicates that the broad-band wave does not contribute significantly to the motions, which are dominated by scattered energy (noise).

The examination of spatial variability by means of the methodology developed herein recognizes correlation patterns in the amplitude and phase variation of motions recorded over extended areas, which

were not observed earlier with the use of conventional approaches. The application of the method to additional sites and earthquake magnitudes, the mathematical representation of the identified correlations in the amplitude and phase variations and their quantitative association with physical characteristics, and the further investigation of the spatially variable arrival time perturbations are currently underway.

ACKNOWLEDGEMENTS

This study was supported by the National Science Foundation (NSF) under Grant No. BCS-9114895. The SMART-1 array data were made available by the Seismographic Station of the University of California at Berkeley and the Institute of Earth Sciences of the Academia Sinica in Taipei. The authors wish to thank Prof. Athina Petropulu of the Electrical and Computer Engineering Department at Drexel University for her suggestions on signal processing techniques, and Dr. Paul Spudich of the U.S. Geologic Survey, Menlo Park, CA, for his constructive comments on this work.

REFERENCES

1. P. Spudich, 'Recent seismological insights into the spatial variation of earthquake ground motions', in *New Developments in Earthquake Ground Motion Estimation and Implications for Engineering Design Practice*, ATC, 35-1, 1994.
2. N.A. Abrahamson, B.A. Bolt, R.B. Darragh, J. Penzien and Y.B. Tsai, 'The SMART-1 accelerograph array (1980-1987): a review', *Earthquake spectra*, **3**, 263-287 (1987).
3. N.A. Abrahamson, J.F. Schneider and J.C. Steep, 'Spatial variation of strong ground motion for use in soil-structure interaction analyses', *Proc. 4th U.S.-natl. conf. earthquake eng.*, Palm Springs, CA, 1990.
4. N.A. Abrahamson, J.F. Schneider and J.C. Stepp, 'Empirical spatial coherency functions for applications to soil-structure interaction analyses', *Earthquake spectra* **7**, 1-27 (1991).
5. H. Hao, C.S. Oliveira and J. Penzien, 'Multiple-station ground motion processing and simulation based on SMART-1 array data', *Nucl. eng. des.*, **111**, 293-310 (1989).
6. R.S. Harichandran, 'Local spatial variation of earthquake ground motion', in J.L. Von Thun (ed.), *Earthquake Engineering and Soil Dynamics II-Recent Advances in Ground Motion Evaluation*, Geotechnical Special Publication No. 20, ASCE, New York, 1988.
7. R.S. Harichandran and E.H. Vanmarcke, 'Stochastic variation of earthquake ground motion in space and time', *J. eng. mech. div. ASCE* **112**, 154-174 (1986).
8. C.H. Loh, 'Analysis of the spatial variation of seismic waves and ground movements from SMART-1 data', *Earthquake eng. struct. dyn.*, **13**, 561-581 (1985).
9. W. Menke, A.L. Lerner-Lam, B. Dubendorff and J. Pacheco, 'Polarization and coherence of 5-30 Hz seismic wave fields at a hard rock site and their relevance to velocity heterogeneities in the crust', *Bull. seism. soc. Am.*, **80**, 430-449 (1990).
10. O. Ramadan and M. Novak, 'Coherency functions for spatially correlated seismic ground motions', *Geotechnical Research Centre Report No. GEOT-9-93*, The University of Western Ontario, London, Canada, 1993.
11. J.F. Schneider, J.C. Stepp and N.A. Abrahamson, 'The spatial variation of earthquake ground motion and effects of local site conditions', *Proc. 10th world conf. earthquake eng.*, Madrid, Spain, 1992.
12. P.G. Somerville, J.P. McLaren, C.K. Saikia and D.V. Helmberger, 'Site-specific estimation of spatial incoherence of strong ground motion', in J.L. Von Thun (ed.), *Earthquake Engineering and Soil Dynamics II-Recent Advances in Ground Motion Evaluation*, Geotechnical Special Publication No. 20, ASCE, New York, 1988.
13. A. Zerva, 'Seismic ground motion simulations from a class of spatial variability models', *Earthquake eng. struct. dyn.*, **21**, 351-361 (1992).
14. N.A. Abrahamson, 'Spatial interpolation of array ground motions for engineering analysis', *Proc. 9th world conf. earthquake eng.*, Tokyo, Japan, 1988.
15. N.A. Abrahamson, 'Generation of spatially incoherent strong motion time histories', *Proc. 10th world conf. earthquake eng.*, Madrid, Spain, 1992.
16. O. Zhang and A. Zerva, 'Analysis and synthesis of seismic ground motions. Part II: Applications to SMART-1 array data', *Research Series Report No. 95-01*, Department of Civil Engineering, Drexel University, Philadelphia, PA, 1995.
17. A. Zerva and O. Zhang, 'Analysis and synthesis of seismic ground motions. Part I: Methodology and examples', *Research Series Report No. 94-01*, Department of Civil Engineering, Drexel University, Philadelphia, PA, 1994.
18. N.A. Abrahamson and B.A. Bolt, 'Array analysis and synthesis mapping of strong seismic motion', in B.A. Bolt (ed.), *Seismic Strong Motion Synthetics*, Academic Press, New York, 1987.
19. J. Capon, 'High-resolution frequency-wavenumber spectrum analysis', *Proc. IEEE*, **57**, 1408-1418 (1969).
20. R.B. Darragh, 'Analysis of near-source waves: separation of wave types using strong motion array recordings', *Ph.D. thesis*, University of California, Berkeley, CA, 1987.
21. P. Spudich and D. Oppenheimer, 'Dense seismograph array observations of earthquake rupture dynamics', in S. Das, J. Boatwright and C.H. Scholz (eds), *Earthquake Source Mechanics*, Geophysical Monograph 37, American Geophysical Union, Washington, D.C., 1986.
22. O. Zhang, *Ph.D. thesis*, Department of Civil Engineering, Drexel University, Philadelphia, PA, in preparation.
23. A. Der Kiureghian, 'Model for coherency function for spatially varying ground motion', *Proc. 5th U.S. natl. conf. earthquake eng.*, Chicago, IL, 1994.